Unraveling the Dusty Environment Around RT Vir

MICHAEL D. PRESTON, ANGELA K. SPECK, SEAN DILLON, AND BETH SARGENT 2,3

¹ University of Texas at San Antonio

1 UTSA Circle
San Antonio, TX 78249, USA

² Department, Space Telescope Science Institute
3700 San Martin Drive
Baltimore, MD 21218, USA

³ John's Hopkins University
3400 N Charles Street
Baltimore, MD 21218, USA

ABSTRACT

Infrared studies of asymptotic giant branch (AGB) stars are critical to our understanding of the formation of cosmic dust. In this investigation, we explore the mid-to-far-infrared emission of oxygenrich AGB star RT Virginis. This optically thin dusty environment has unusual spectral features when compared to other stars in its class. To explore this enigmatic object we use the 1-D radiative transfer modeling code DUSTY. Modeled spectra are compared with observations from the Infrared Space Observatory (ISO), InfraRed Astronomical Satellite (IRAS), the Herschel Space Observatory and a host of other sources to determine the properties of RT Vir's circumstellar material. Our models suggest a set of two distant and cool dust shells at low optical depths ($\tau_{V,\text{inner}} = 0.16$, $\tau_{V,\text{outer}} = 0.06$), with inner dust temperatures: $T_1 = 330$ K, $T_3 = 94$ K. Overall, these dust shells exhibit a chemical composition consistent with dust typically found around O-rich AGB stars. However, the distribution of materials differs significantly. The inner shell consists of a mixture of silicates, Al_2O_3 , FeO, and Fe, while the outer shell primarily contains crystalline Al_2O_3 polymorphs. This chemical change is indicative of two distinct epochs of dust formation around RT Vir. These changes in dust composition are driven by either changes in the pressure-temperature conditions around the star or by a decrease in the C/O ratio due to hot-bottom burning.

Keywords: Circumstellar dust(236) — Dust shells (414) — Infrared astronomy(786) — Asymptotic giant branch stars (2100) — Dust formation (2269) — Radiative transfer simulations (1967)

1. INTRODUCTION

Understanding the nature and formation of cosmic dust is critical to understanding most cosmic environments. Infrared (IR) Astronomy has shown that dust contributes to the physics of star and planet formation, mass loss from evolved stars, interstellar gas heating, and the formation of molecules (e.g. Draine 2003; Krishna Swamy 2005; Woitke 2006; Krügel 2008).

In our galaxy, some of the most important dust formation regions are around Asymptotic Giant Branch (AGB) stars (Kwok 2004). AGB stars evolve from low-to-intermediate mass main-sequence stars ($0.8-8M_{\odot}$). Pulsations and shocks propagating through the upper atmospheres of AGB stars lift material off the stellar

surface, creating expanding shells of material around the star (Höfner et al. 2016). The environment in these shells is relatively cool with little ultraviolet (UV) radiation from the star, making it ideal for the formation of molecules and condensation of dust grains. The dust grains are higher in opacity, and thus are more susceptible to radiation pressure from the star. As these dust grains are driven away from the star, they drag the gas along with them. This circumstellar material continues to move away from the star, and can form shells of coupled gas & dust around the central star (Höfner 2009).

Dust chemistry in these circumstellar outflows is dictated by the abundance of carbon and oxygen in the outflow. Carbon and oxygen will preferentially form

Table 1. Table of basic properties of RT Vir

Property	Value	Reference
Spectral Type	M8III	1
Variability Type	SRb	2
Period (days)	153 - 320	3
Mass-loss rate $(\dot{M}/\mathrm{M}_{\odot}\mathrm{yr}^{-1})$	$10^{-7} - 10^{-6}$	4, 5
CO expansion velocity $(v_{\rm gas})$	$7.8, 11.3 \mathrm{km s^{-1}}$	6, 7
Luminosity (L_{\star}/L_{\odot})	$5012^{+1,154}_{-938}$	5
Stellar temperature (T_{eff}, K)	2902	8
Maser emission type	H_2O	9, 10
Hipparcos Distance	$135\pm15\mathrm{pc}$	11
GAIA/VLTI Distance	$226\pm7\mathrm{pc}$	12, 13

References: (1) Joy (1942); (2) van der Veen et al. (1995); (3) Kudashkina & Andronov (2022); (4) Imai et al. (2003); (5) Brand et al. (2020); (6) Olofsson et al. (2002) (7) Loup et al. (1993); (8) Sharma et al. (2016) (9) Bains et al. (2003); (10) Kim et al. (2010); (11) van Leeuwen (2007); (12) Zhang et al. (2017); (13) Andriantsaralaza, M. et al. (2022).

neutral CO gas, sequestering the less abundant element and restricting the chemistry of the molecules and dust grains that form later. Consequently, if C is more abundant than O, the primary dust chemistry will be C-rich, and grains of SiC, graphite (or amorphous C) and other C-bearing minerals will form. Conversely, O-rich stars will form silicate minerals ((SiO₄)⁻⁴ tetrahedra-bearing) and metal-oxides (Al₂O₃, FeO, etc.) In systems like these (C rich or O rich), grain condensation is not fully understood (e.g. Woitke 2006; Höfner 2009). In the interest of exploring dust production in O-rich AGB outflows we investigate the dusty environment around the star RT Virginis (RT Vir).

1.1. RT Virginis

RT Vir is an AGB star first described by Williamina Fleming (Pickering & Fleming 1896), and its vital statistics are given in Table 1. RT Vir is a target in many studies of astrophysical maser emission and in several surveys of AGB and semiregular (SR) variable stars. The circumstellar emission has been studied extensively through imaging in the IR (via the Herschel & AKARI Space Observatories; Pilbratt et al. 2010; Kawada et al. 2007) and the ultraviolet (UV; via the Galaxy Evolution Explorer, GALEX; Martin et al. 2005) (e.g., Groenewegen et al. 2011; Mayer et al. 2011; Cox et al. 2012; Sacuto et al. 2013; Paladini et al. 2017; Sahai & Stenger 2023). These studies lend a great deal of insight into the properties of AGB stars in general and specifically RT Vir. However, there is a dearth of investigations into this star's circumstellar dust spectroscopy in the mid-to-far-IR. Observations of RT Vir at mid-IR wavelengths show

unusual emission features between 9-40 μ m as shown in Figure 1. To make a fair comparison to other AGB star spectra, we selected only those objects classified as SE3t in Sloan & Price (1998), with spectral types later than M6.5III and variability type SRb. However, since only two such objects met these criteria and had available ISO SWS spectra, we also included two additional stars: SE2t star, Y UMa, and SE3 star RX Vul. RX Vul is a Mira variable rather than a SR type, but the SE3 class (without the 13 μ m feature) only includes 4 stars so the choices were sparse. We also included data from Figure 1 of Sloan et al. (2003) that depicts an averaged spectrum of stars with SE3 dust emission, and little to no emission at $13 \,\mu\text{m}$. AGB stars exhibit a wide range of spectral features (e.g., Speck et al. 2000; Little-Marenin & Little 1988; Sloan et al. 2003), so these measures were taken to minimize spectral differences between the selected stars and RT Vir.

In Figure 1, for RX Boo, SV Peg and Y Uma we see significant IR enhancement at ~ 10 and $18 \,\mu\mathrm{m}$ due to warm silicates, and some other features at ~ 13 , 20, $21 \,\mu \text{m}$ correlated with other oxides present in the circumstellar environment. RX Vul shows a strong enhancement at $\sim 10 \,\mu\mathrm{m}$ but lacks the emission features at 13, 20 and 21 μ m associated with oxides. While the spectrum of RT Vir does exhibit features in the mid- and far-IR, they are unlike those seen in the comparison Orich AGB stars. Figure 1 also shows that RT Vir lacks a pronounced 13 μ m feature, instead showing a "bridge" of emission between features at 10 and 20 μ m. Additionally, this "bridge" emission distinguishes RT Vir from SE3 class stars like RX Vul which also lacks a 13 μm feature. This demonstrates oddity, even allowing for the intrinsic variation within this class of objects. This deviation from the classical O-rich AGB dust shell features makes RT Vir an even more interesting object to

Here we present new radiative transfer models of this unusual AGB star. In § 2 we describe from whence the observation data were collected. In § 3, we describe the methodology used to produce radiative transfer models that fit well to the observations. In § 4 we provide the results of the modeling, and § 5 discusses the implications and interpretation of the modeling results in terms of dust composition, the large extent of the dust shell, and mass-loss timescales. Conclusions are drawn in § 6.

2. OBSERVATIONS

We have obtained photometric observations from UV to IR wavelengths for RT Vir from multiple sources including Simbad(Ducati 2002) and IRSA. We also collected fully processed post-pipeline spectral data from

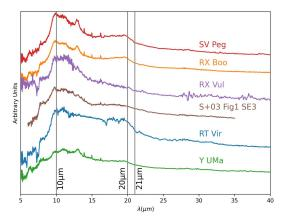


Figure 1. Comparison of mid-infrared photosphere-subtracted ISO-SWS spectra of RT Vir with similar types of stars, SV Peg, RX Boo, RX Vul and Y UMa, along with the average SE3 class spectrum (without a $13\,\mu\mathrm{m}$ feature) presented by Sloan et al. (2003). For the individual stars, the photosphere subtraction uses a model M5 III-Star template courtesy of Kevin Volk, described in § 2. The ISO spectra used in Sloan et al. (2003) to generate their SE class averages where also stellar subtracted, but using ISO data for NU Pav, a naked M6 III-star and the photosphere to be subtracted

the Infrared Space Observatory's Short Wavelength Spectrometer (ISO SWS; Kessler et al. 1996; de Graauw et al. 1996), which were acquired from an online atlas¹ associated with Sloan et al. (2003). The resulting spectral energy distribution (SED) of RT Vir is shown in Figure 2, while the photometric observations are listed in Table 5 in the Appendix. The vertical spread in photometry points is attributable to the intrinsic variability of RT Vir. Also included in Figure 2 are labels for the locations of prominent molecular absorption features in the near- to mid-IR, the precise wavelengths for which are listed in Table 2. The molecules that cause these absorption features occur both in the stellar photosphere and in the circumstellar outflow. For this reason, we have included in the figure a template stellar spectrum (blue line) which we will use in radiative transfer modeling (see § 3). Our stellar spectrum template (courtesy of Kevin Volk) is compiled from a collection of observations. In the infrared ISO SWS and LWS data for several M5III stars were compiled, giving high-resolution data from $2-200 \,\mu\text{m}$. The visible observations were sourced from Pickles (1985). The discrepancy between the tem-

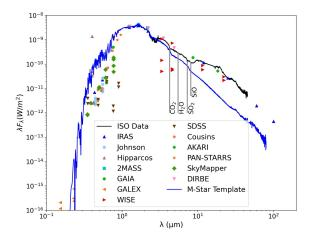


Figure 2. Spectral Energy Distribution (SED) for RT Vir. The dark line is spectroscopy from ISO SWS, and the solid blue line is the M Star template described in the text. All other marks are photometry measurements from various surveys performed at different times. The large spread in brightness at a given wavelength are a result of the variable nature of RT Vir. Grey vertical lines indicate positions of molecular absorption bands in RT Vir's atmosphere

plate and the observed SED at $\lambda > 8 \,\mu \text{m}$ arises from the dust excess, which we model in this study. At $\lambda < 1, \mu m$, the poor fit is primarily due to a mismatch in spectral type: RT Vir is an M8III star, whereas the template spectra correspond to M5III stars. The higher temperature of M5 ($T_{\rm eff} \sim 3400 \, {\rm K}$, Perrin et al. 1998) stars compared to M8 ($T_{\rm eff} \sim 2800 \, {\rm K}$) stars significantly affects the short (visible/UV) wavelengths, resulting in the lower observed fluxes at visible wavelengths. In contrast, the mid-IR differences are much less pronounced. Since our modeling primarily focuses on IR wavelengths, achieving a precise fit at visible and UV wavelengths is not critical. It is also worth noting that it is almost impossible to find a reference for a reliable list of wavelengths and line widths simply because of the complex nature of molecular spectra. This problem is exacerbated by the fact that the CO, H₂O, and SiO absorption features in the $3-10 \,\mu\mathrm{m}$ range are broad and overlap, sometime merging into a single broader absorption region (e.g., Gustafsson 1998), as seems to be the case for RT Vir. The references quoted in Table 2 provide some wavelengths or ranges for specific molecular species.

3. MODELING

We use the one-dimensional Radiative Transfer (RT) modeling code DUSTY 2.07 (Ivezic & Elitzur 1995; Nenkova et al. 1999) to generate model SEDs for RT Vir. DUSTY solves the RT equation along the line of sight

Detailed data reduction information is available from the atlas website: https://users.physics.unc.edugcsloan/library/swsatlas/ aot1.html.

Table 2. Wavelengths of mid-infrared molecular absorption features

Molecule	Wavelengths (μ m)
CO	1.4, 2.3, 4.6
H_2O	1.5, 1.9, 2.7, 6.2
SiO	8.2
SO_2	7.3
CO_2	4.26, 13.49*, 13.87*, 14.98, 16.18*, 16.78

^{*}Emission features

Gustafsson (1998); Matsuura et al. (1999); Yamamura et al. (2000); Sloan et al. (2015)

in one dimension based on a sequence of user-defined initial parameters (Ivezic & Elitzur 1995). We compare the model DUSTY SEDs with observed spectral data for RT Vir (Figure 2) to generate as accurate a model of the dust environment as possible.

DUSTY allows us to adjust the nature of the central star, as well as the size, optical depth (τ_V) , inner dust temperature (T_{inner}) , density distribution and composition of the simulated dust shell. DUSTY provides us multiple ways to input the spectrum of a stellar photosphere. We can use a simple blackbody spectrum, or we can use a 'naked' stellar atmosphere model. Model stellar atmospheres have the advantage that the strong molecular absorption bands that are used to classify cool stars are already present in the spectrum prior to passing light into our simulated dust shell. As described in § 2 we use a stellar spectrum template created from observations of M5III stars.

Our starting assumption for the radial density distribution is that it follows r^{-2} , which would reflect a constant mass-loss rate. Current dust formation models suggest that mass loss from AGB stars is influenced by several factors, particularly the pulsation cycle (Höfner et al. 2016, and references therein), which may lead to periodic enhancements in dust density or clump formation (e.g., Freytag & Höfner 2023). However, Villaver et al. (2002a,b) showed that hydrodynamic processes in the circumstellar shell erase such density structures, resulting in a r^{-2} density distribution. Deviations from r^{-2} will be described below.

Our free parameters for modeling RT Vir are, therefore, τ_V (related to the absolute dust density), T_{inner} , and the composition of the simulated dust shell. DUSTY includes both built in dust species, and an external library of complex refractive indices corresponding to a variety of materials, which we can supplement from the literature. While we used a range of silicate and oxide mineral optical constants, our best fitting models used the complex refractive indices of the following user-

defined species: Updated 'cosmic' silicate and metallic iron from Speck et al. (2015), iron oxide from Henning et al. (1995), amorphous Al_2O_3 from Begemann et al. (1997), and crystalline Al_2O_3 from Pecharromán et al. (1999).

The crystalline Al_2O_3 refractive indices were generated from vibrational parameters of annealed hydrous aluminum oxides published by Pecharromán et al. (1999). The initial minerals were bayerite (monoclinic polymorph of gibbsite: β -Al(OH)₃) & boehmite (AlO(OH)). Pecharromán et al. (1999) heated each material at various temperatures and modeled their vibrational parameters, from which we were able to calculate the complex refractive indices of the resultant materials. The annealing experiments by Pecharromán et al. (1999) generated final samples composed of multiple crystalline polymorphs of Al_2O_3 (e.g., α -, δ -, γ -, η -, θ) in different combinations depending on the initial sample and the annealing temperature.

Our initial modeling assumed a single, continuous dust shell in which the composition is the same throughout, and using the M Star template for the stellar photosphere. Using a mixture of cosmic glass, amorphous-Al₂O₃, Fe, and FeO, we could match the observational data shortwards of $\sim 22 \,\mu\mathrm{m}$, but beyond that wavelength, the model begins to fail, being too low in flux and not matching the observed 28 and $32 \,\mu\mathrm{m}$ features. Increasing the amount of the coolest dust by modifying the radial density distribution led to unrealistic density profiles. Molster et al. (2002a) and Molster et al. (2002b) showed that forsterite (Mg₂SiO₄, the Mg-rich end-member of the olivine series of minerals) can be associated with emission features at 28 & 32 µm. Therefore, to match the 28 and $32 \,\mu\mathrm{m}$ features we employed both forsterite, and fayalite (Fe₂SiO₄, the Fe-rich end member of the olivine series). Adding either of these minerals resulted in overestimation at shorter wavelengths and while features appeared near 28 and 32 μ m, the precise shapes of these features were too tall and narrow to match observations from ISO SWS.

Sargent (2018) examined a set of AGB stars with similar $28-32 \,\mu\mathrm{m}$ features, and successfully modeled those features using the crystalline $\mathrm{Al_2O_3}$ refractive indices from Pecharromán et al. (1999). They found that the $28-32 \,\mu\mathrm{m}$ features in their models were highly sensitive to the shape of the dust grains. By default, DUSTY assumes spherical dust grains. However, it is possible to simulate the effects of light interacting with dust of different shapes, by computing the absorption and scattering cross sections ($\mathrm{C_{abs}}$ and $\mathrm{C_{sca}}$) of such dust outside of the DUSTY program. We have written a python program based on work in Min et al. (2003); Fabian et al.

(2001) & Bohren & Huffman (1998) that generates the absorption and scattering cross sections for grains in a continuous distribution of ellipsoids (CDE;Dillon et al. 2025 in prep.). We tested each annealed sample from Pecharromán et al. (1999) individually, and found that the products of bayerite annealed at 1273 K provide the best fit to the position and shape of features at 28 & $32 \,\mu\text{m}$. Unfortunately, this material also resulted in flux overestimation at shorter wavelengths (like the olivine grains), which is consistent with expected behavior of crystalline Al_2O_3 (Sloan et al. 2003).

To model the 28 and 32 μ m features, we needed a gradient in composition with distance from the star. Introducing a gradient allowed us to include cool dust species that contribute emission features at 28 and 32 μ m without incurring too much emission at shorter wavelength. Since DUSTY does not allow a user-input compositional gradient in a single model, we generated a two-shell model to simulate a change in composition over radial distance. We use the SED for the best-fitting single-shell model described above to replace the M Star template as the input spectrum, and we ran another set of models. The output from this method returns a single model of two dust shells which can have different inner temperatures, different sizes, compositions, and optical depths. To avoid confusion, from this point forward we will use R_1, R_2, R_3, R_4 to refer to the inner boundary of the inner shell, outer boundary of the inner shell, inner boundary of the outer shell and outer boundary of the outer shell respectively (see also Table 3 and Figure 3).

DUSTY limits the input of absorption and scattering cross-sections to a single input file that comprises all the types of dust. Because of this limitation, the second shell models used CDE grains of a single size and composition for each model attempt. We first tried to fit features at 28 and 32 μ m with the crystalline silicates fayalite and forsterite; while we eliminated the overestimation of flux at short wavelengths, the 28 and 32 μ m features were still too sharp. Using the annealed bayerite from Pecharromán et al. (1999) (with CDE grain) shapes provided the best fit to the 28 and 32 μ m in the ISO SWS spectrum.

Model fits were judged first by visually assessing the shape of the modeled SED (see Figure 4 & 5). Visual assessment is needed due to the difficulty of applying mathematical goodness of fit methods (e.g., χ^2 fitting). Since DUSTY ingests only input parameters and does not physically simulate the system, fully automating DUSTY may return unphysical results, or potentially minimize χ -squared by glossing over smaller features. Additionally, molecular features that are present in observation could skew the model output, and DUSTY

Table 3. Parameters of the best fit DUSTY model. Sources for the optical properties of each dust species are listed below. Optical depth (τ_{λ}) is evaluated at V-band $(0.55 \,\mu\mathrm{m})$.

Shell 1 Value	Shell 2 Value				
Fractional Abundances					
0.380	0.00				
0.217	0.00				
0.00	1.00				
0.163	0.00				
0.239	0.00				
Other Parameters					
330^{+30}_{-20}	94^{+16}_{-5}				
$0.16 {\pm} 0.02$	$0.06 {\pm} 0.02$				
$(R_1) 150^{+20}_{-25}$	$(R_3) 550^{+65}_{-210}$				
$(R_2)300^{+40}_{-50}$	$(R_4) 10950^{+1200}_{-4300}$				
	onal Abundance 0.380 0.217 0.00 0.163 0.239 ner Parameters 330^{+30}_{-20} 0.16±0.02 (R ₁) 150 ⁺²⁰ ₋₂₅				

^a Speck et al. (2015), ^b Begemann et al. (1997), ^c Pecharromán et al. (1999); the annealed bayerite is actually a mixture of Al_2O_3 polymorphs, dominated by the α- and θ-structures, and does not contain any residual bayerite. ^d Henning et al. (1995). ^e Assuming GAIA distance from Table 1.

does not model molecular gas features. As discussed in § 2, the M star template used to simulate the stellar photosphere is hotter than RT Vir, resulting in a slightly brighter modeled SED at visual and UV wavelengths compared to observations. However, emission longward of $\sim 1\,\mu\mathrm{m}$ matches well.

To further assess the goodness of fit of our models, we subtract the model from the observed SED and plotted the residuals, shown in Figure 6. This plot allows us to represent the ISO SWS spectrum as a straight line, and further assess where our model fits well, and where it does not. As mentioned above, DUSTY does not model the molecular features present in the SED. These features cause our model to over/underestimate emission, in the 5-9 μ m range, depending on the stellar template used. With this in mind, we will focus our modeling efforts on the part of the SED dominated by the infrared excess from dust at wavelengths greater than $\sim 8 \, \mu$ m.

4. MODEL RESULTS

Our best fitting DUSTY model for RT Vir is shown in Figures 4 & 5 with residuals in Figure 6 and the DUSTY model parameters are given in Table 3. These parameters indicate the presence of a highly extended, optically thin dust shell consisting of two distinct layers as shown schematically in Figure 3. Figure 5 shows the model fit to the ISO SWS spectrum focused on the star's IR dust excess $(8\mu m \le \lambda \le 40\mu m)$. Figure 6 shows the residual plots for the same model shown in Figure 5 over the same

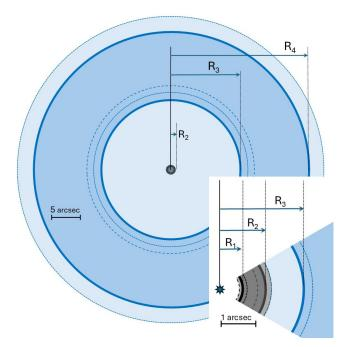


Figure 3. Schematic view of the two-shell DUSTY model. The inner dust shell is depicted in grey and black; the outer dust shell is depicted in blue. The thick arcs represent the nominal boundaries (inner and outer radius of each dust shell), while the dashed lines depict the minimum and maximum positions of those boundaries (longer dashes = minimum, shorter dashes = maximum). The darker grey and mid blue areas are the dust shells using the nominal boundary radii; the paler grey and blue mark the potential extent of each shell based on the minimum and maximum sizes. R₁ is the inner dust radius for the inner dust shell; R2 is the outer dust radius for the inner dust shell; R₃ is the inner dust radius for the outer dust shell; R4 is the outer dust radius for the outer dust shell. Inset is an enlargement of the inner regions to show the inner dust shell details. Scale bars are based on the GAIA distance of 2.26 pc.

range of wavelengths. This figure was used to assess the goodness of fit for our model SED, and highlights where the model either over or underestimates emission. The grey lines in both Figure 6 & 5 indicate the positions of well known dust features. In our model of the inner shell, the largest fraction of dust is made up of cosmic silicates with smaller fractions of Al₂O₃, Fe, and FeO. The dust temperature, T_1 at the inner radius, R_1 , of the dust shell is 330 K. In the model of the outer shell, composition is held constant at 100% annealed bayerite (from Pecharromán et al. 1999), which consists of a mixture of Al₂O₃ polymorphs, with θ - and α -Al₂O₃ having the greatest fractional abundance in the sample. Inner temperature, T_3 at the inner radius, R_3 , of this shell is 94 K. This dust is particularly cool; and since DUSTY calculates dust shell radius using the inner dust temperature (T_{inner}) the calculated shell sizes are large as

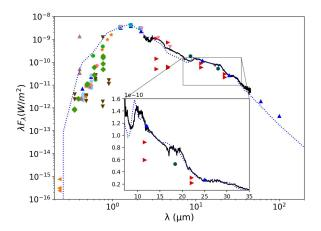


Figure 4. Best fitting DUSTY model SED for RT Vir. Photometric points (colors) and ISO-SWS spectrum (black solid line) are identical to Figure 2. Blue dotted line is the best fitting modeled SED with parameters as listed in Table 3. Inset zooms into the mid-IR region $(5-35 \,\mu\text{m})$ to show the details of the fit to the dust features

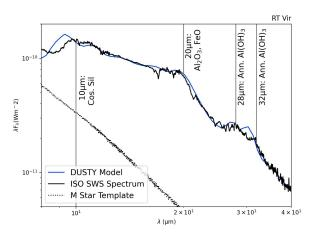


Figure 5. DUSTY model spectra for RT Vir. Model spectra (blue) are fit to observed data (ISO SWS data in black) with important dust features highlighted by vertical grey lines (cosmic silicates, Al₂O₃, FeO, and annealed Bayerite). The black dotted line shows the stellar template used to calculate the model.

a result (see \S 5.5 for complete discussion of pressure-temperature parameter space for this star).

It is worth noting that while the nominal positions of the dust layers leaves a gap of a few hundred AU between the inner and outer shells, if we assume the maximum extent for the inner shell (R_2 is at maximum) and the minimum distance for the inner boundary of the outer shell (R_3 is at minimum), then $R_2 = R_3$ and we have a

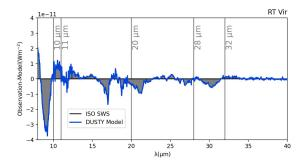


Figure 6. Residuals from the best fitting model above: Model(blue); ISO data (black). Vertical lines denote the same important features that are highlighted in Figure 5. The discrepancies are discussed in § 5

continuous dust shell, although the composition changes at this point (see Figure 3).

5. DISCUSSION

5.1. Dust Composition

Based on the results of our RT modeling, RT Vir has circumstellar dust that is distant and cool. The dust cloud itself is relatively optically thin, with $\tau_V \approx 0.16$.

We successfully model the overall shape of both the SED and most prominent dust features at 10, 11, 18-20, and $28\text{-}32\,\mu\text{m}$, as well as the broad emission 'bridge' between $\sim\!10$ and $20\,\mu\text{m}$. In O-rich systems, emission at 10 and $18\,\mu\text{m}$ is associated primarily with warm silicate grains. Other common features at $11\,\mu\text{m}$, $13\,\mu\text{m}$, $20\,\mu\text{m}$ are associated with two polymorphs of Al_2O_3 and FeO (Speck et al. 2000; Sloan et al. 2003). Features at $28\text{-}32\,\mu\text{m}$ are often associated with crystalline grains, and in this case best modeled by a mixture of crystalline Al_2O_3 polymorphs.

Studies of dust around O-rich AGB stars have revealed multiple classes of AGB stars (e. g. Little-Marenin & Little 1988; Sloan & Price 1998; Speck et al. 2000). RT Vir, however, does not fit cleanly into any of these classifications. The dust features for RT Vir are broad and don't present clear peaks, but remain different from the classic "broad" feature described by Little-Marenin & Little (1990); Speck et al. (2000). In spite of this notable difference, we have produced a successful model using the commonly expected astrominerals described above. The key differences for RT Vir's model parameters are the cool dust and vast shell size.

5.2. Large extent of the modeled dust shell

The large extent of the model may seem surprising but is consistent with imaging observations of RT Vir at multiple wavelengths. The Herschel Space Observatory PACS instrument observed RT Vir in the 70 and $160 \,\mu\mathrm{m}$ bands in 2010 as part of the MESS (Mass-loss of Evolved StarS) Herschel key program (Groenewegen et al. 2011). The 70μ m-image is shown in Figure 7 depicting far-IR emission up to $\sim 3'$ away. Cox et al. (2012) modeled AGB stars from the MESS Key Program and found that RT Vir has a wind-ISM interaction region with pronounced Kelvin-Helmholtz instabilities, and a general "fermata" shape or \bigcirc (this is a musical symbol that strongly resembles the bow shock and star combination). Cox et al. (2012) modeled the standoff-distance between this bow shock and the star at 2.6'. The dense bow-shock emission at $70 \,\mu m$ shows an angular separation of 2.9' at the extreme edge of the densest emission along the bow shock (see Figure 7) . This fermata shape is indicative of having a leading bow-shock formed as the stellar wind collides with the ISM in the direction of the proper-motion of the star (see, e.g., Wareing et al. 2006).

The extent of the RT Vir dust shell in these observations translates to a shell size of $\sim 40,000\,\mathrm{AU}$ assuming the GAIA distance from Table 1. RT Vir has also been found to be extended at other wavelengths. The 2 Micron All Sky Survey (2MASS; Skrutskie et al. 2006) took images in the J, H, and K bands; the K-band image shows extended gas and dust emission $\sim 2' \ (\sim 27,000 \, \mathrm{AU})$ away. Sahai & Stenger (2023) used GALEX observations of RT Vir to show the bow shock and astrotail of the star align with its proper motion vector. Thus RT Vir is extended in UV wavelengths. RT Vir has also shown extended emission in images from AKARI (Ueta et al. 2018), and the Spitzer Space Telescope (unpublished). All these observations suggest dust and gas extends at least twice as far as our modeled outer dust shell. With the most recent distance estimates to RT Vir (~226±7 pc Zhang et al. 2017; Andriantsaralaza, M. et al. 2022), the outer extent of our modeled dust shell should appear around 48'' ($\sim 0.8'$). Our models are therefore not unreasonable.

5.3. Drift Velocity

For what follows in § 5.5–§ 5.7, we need to discuss the outflow speeds, which impact calculations of timescales and pressure-temperature regimes. Although we use the gas outflow velocity as measured from CO observations (Loup et al. 1993; Olofsson et al. 2002), this may not be identical to the dust outflow velocity. The prevailing hypothesis for outflows from AGB stars is that dust forms in the stellar atmosphere and is propelled outward by radiation pressure from the star's luminosity. As the dust accelerates, it transfers momentum to the molecular and atomic gas through collisions. Consequently, the gas outflow velocity at large distances from the star

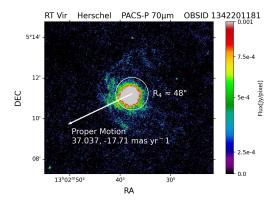


Figure 7. Herschel PACS 70 μ m image of RT Vir, showing the fermata ($\widehat{}$) shaped bow-shock emission that extends to $\sim 3'$ away from the central star. The white arrow indicates the direction of the proper motion of RT Vir. The white circle marks the outer extent of our modeled dust shell ($R_4 \approx 48$ ")

depends on the stellar luminosity (L_{\star}) , the dust-to-gas ratio, the mass-loss rate (\dot{M}) , and the properties of the dust grains. The difference between the gas velocity $(v_{\rm gas})$ and the dust velocity $(v_{\rm dust})$ is known as the drift velocity $(v_{\rm drift})$.

Direct measurements of dust velocity are challenging because the spectral features are too broad to detect Doppler shifts. In contrast, molecular gas, typically observed through CO in radio wavelengths, allows for the determination of both Doppler broadening and the gas mass-loss rate. In general, it is assumed that the drift velocity is not huge and that the dust outflow velocity is similar to gas outflow velocity (e.g., Höfner & Olofsson 2018), the reality depends on the optical depth of the dust shell. For optically thick dust shells, the drift velocity is expected to be negligible (Gail & Sedlmayr 1985). However, the case for optically thin dust shells, like that of RT Vir, is less clear. Direct measurements of dust velocity were achieved by Dougados et al. (1992) using dust-scattered photospheric emission lines in a single object (Frosty Leo, post-AGB object) and found that the dust velocity varies but is consistently 10-20 km s⁻¹ slower than the CO molecular gas velocity, however, they did suggest this could be an artifact of the radiative transfer process. Meanwhile, Goldreich & Scoville (1976) modeled dust around the more optically thick OH-IR star type and found the drift velocity to be $9 \,\mathrm{km \, s^{-1}}$ (dust faster than gas). And Berruyer & Frisch (1983) developed a two-fluid model that produced dust velocities of $\sim 2-4 \,\mathrm{km}\,\mathrm{s}^{-1}$ and gas velocities of 1-2km/s. More recent models have been developed that suggest much higher drift velocities. Sandin et al. (2023) included dust-gas drift into their models for mass loss

from O-rich AGB stars and found $v_{\rm drift}$ could be as high as $300\,{\rm km\,s^{-1}}$, while Zargarnezhad et al. (2023) used a dust-gas-drift modeling technique to investigate the formation of clumps and inhomogeneities in AGB star shells and found $v_{\rm drift}{\approx}30\,{\rm km\,s^{-1}}$ (for $v_{\rm gas}{\approx}11\,{\rm km\,s^{-1}}$). It should be noted that Kwok (1975) stated that $v_{\rm drift}{\gtrsim}20\,{\rm km\,s^{-1}}$ would lead to dust grain destruction via sputtering.

Habing et al. (1994) studied whether the gas outflow velocity could be used to estimate the gas-to-dust ratio, and came up with an equation for the drift velocity in terms of stellar luminosity, mass loss rate, gas velocity and the average radiation pressure efficiency ($\langle Q_{\rm rp} \rangle$, which, in turn, is determined by the nature of the dust grains in terms of their size and opacity). This is identical to the equation derived by Goldreich & Scoville (1976):

$$v_{\text{drift}}^2 = \frac{\langle Q_{\text{rp}} \rangle L_{\star}}{\dot{M}c} v_{\text{gas}} \tag{1}$$

Since the mass-loss rate and luminosity are both expected to increase during the AGB phase (see e.g. van Loon et al. 2005; Vassiliadis & Wood 1993), these should not have a huge effect on the drift velocity, but the nature of the dust grains may change and thus the drift velocity may vary with time. Calculating $\langle Q_{\rm rp} \rangle$ is not straight forward but we can approximate using functions in Draine (1981) which assume either carbon or "astronomical silicate" grains. For silicates we get a $\langle Q_{\rm rp} \rangle \approx 0.1$ for $1\,\mu{\rm m}$ size grains which is consistent with the values calculated from forsterite (Gilman 1969) and adopted by Berruyer & Frisch (1983). Smaller grain sizes give rise to smaller drift velocities.

Based on the opacities listed in Table 1 of Bladh & Höfner (2012), the wavelength-averaged opacity of Al_2O_3 is very similar to that of non-iron-bearing silicates. In comparison, metallic iron and iron-bearing olivine are approximately 30 and 60 times more opaque, respectively, with amorphous carbon being even more opaque. Since $\langle Q_{\rm rp} \rangle \approx 0.1$ is valid for all non-iron bearing minerals, and most of our dust is not iron-bearing or carbonaceous, we can apply Equation 1 and get a dust drift velocity of 7km/s. Our model also includes metallic iron grains, which would exhibit higher drift velocities; however, the overall dust drift velocity is reduced due to the predominance of much smaller grains. We assume an MRN grain size distribution (see Mathis et al. 1977), which has a maximum grain size of $0.25 \,\mu\mathrm{m}$ and follows a power law, resulting in most grains being significantly smaller (5 nm and up). In addition, since we are examining dust in its earliest stages of formation, we expect the predominance of many small grains. For a

Table 4. Timescales for the age of each shell boundary based on CO wind velocities calculated in Loup et al. (1993)

Boundary	Age^a	Temp^b	Radial	Angular	
	(yrs)	(K)	$Distance^b$	size^c	
			(AU)		
inner shell					
R_1	63^{+72}_{-25}	330	150	0.66''	
R_2	125^{+129}_{-53}	238	300	$1.32^{\prime\prime}$	
outer shell					
R_3	229^{+231}_{-131}	94	550	2.42"	
R_4	4590^{+4544}_{-2658}	34	10950	$48.4^{\prime\prime}$	

 $[^]a$ based on v_{gas} from Table 1; b From Table 3; c based on the GAIA distance of 226 pc (Zhang et al. 2017, and Table 1).

discussion comparing grain sizes relevant to AGB stars, see Speck et al. (2009).

Given the variations in modeling and observational results, and that our model assumes an MRN grain size distribution we assume that $v_{\rm dust} = v_{\rm gas}$, but with $\pm 5\,{\rm km\,s^{-1}}$ to account for potential errors in our timescale calculations.

$5.4.\ Mass-Loss\ Timescales$

While the timescale associated with cooler inner dust temperatures (~100s of years) have periods too long to measure on human timescales, we can observe the shells of dust around the star, and examine the history of its outflow.

Using the GAIA distance of 226 pc (Zhang et al. 2017, and Table 1) and the CO gas expansion velocity (v_{gas}) of 11.3 km s⁻¹ from Loup et al. (1993), we have calculated the timescales associated with the two distinct dust shells, which are listed in Table 4. The errors quoted are based on those from Table 3 plus allowing for a drift velocity v_{drift} of $5 \, \text{km s}^{-1}$, which we discuss in more detail in § 5.3.

Table 4 shows that the size of our modeled dust shells correspond to several hundred years of different dust outflows. These separate epochs of dust formation could represent two periods of dusty outflow followed by an extended period of no or low dust production leading up to the present. It should also be noted that the dust accelerates as it moves away from the star, reaching a terminal velocity some time later (e.g. Habing et al. 1994). This means that the ages calculated here, which assume a constant outflow velocity, are minimum age estimates for each dust shell.

The timescale for the formation of discrete dust shells suggested by our models is of the order of hundreds of years. This matches neither the pulsation timescale (hundreds of days) or the thermally pulsing timescale $(10^4 - 10^5 \text{ years})$. However there are several carbon-rich AGB and post-AGB systems that exhibit discrete dust shells on similar times scales to those from our models. LL Peg (an "extreme" C-rich AGB star, also known as AFGL 3068) has a stunning pinwheel structure of dust density that has a timescale of ~800 yrs between dust shells (Morris et al. 2006; Mauron & Huggins 2006). Similarly, CIT 6 has a pinwheel structure observed in the molecular gas (HC₃N), which has timescales for massloss changes in the 400–1200 yr range (Claussen et al. 2011). A similar multi-ringed shell was observed in molecular gas around C-star, V Hya, with timescales in the hundreds of years Sahai et al. (2022). Meanwhile, the archetypal carbon star, IRC+10216 was observed to have discrete dust rings in V band too (Mauron & Huggins 2010). Post-AGB object AFGL 2688 (a.k.a. the Egg Nebula; Sahai et al. 1998) also exhibits episodic mass loss, with dust shells that formed every 150-450 yrs, for a duration of 75-200 yrs. Finally, Randall et al. (2020) showed that O-rich AGB star, GX Mon, has a broken spiral shell structure extending out to 4000 AU, as measured in molecular gas. Although there is a paucity of similar structures around O-rich mass-losing stars, the C-rich object demonstrate that AGB stars often have dust shells with timescales in the hundreds of years. And GX Mon demonstrates that similar structures are possible for O-rich AGB stars.

5.5. Pressure-Temperature Space

Figure 8 shows the Pressure-Temperature (PT) diagram for RT Vir, where the pressures and temperatures are calculated using mass-loss rate (\dot{M}) and CO gas expansion velocities (v_g) listed in Table 1. The calculations follow the methodology from Speck et al. (2009). Where the dark RT Vir lines intersect dashed and dotted stability lines for condensates indicates the temperature at which said condensates should first become stable (assuming thermodynamic equilibrium). We can see that different minerals should become stable at different pressures and temperatures within the PT space bounded by the mass-loss rate range. The lowest temperature silicate should become stable above $\sim 1000 \, \mathrm{K}$ and metallic iron above $\sim 900 \, \mathrm{K}$. However, our models suggest far cooler dust temperatures, near $\sim 330 \, \mathrm{K}$.

In § 5.6, we will discuss dust formation in more detail but it is important to note that the dust formation temperatures predicted above, which assume thermodynamic equilibrium, should be considered an upper limit. Dust condensation is expected to occur in the 800–1000 K range, and this can be accommodated in

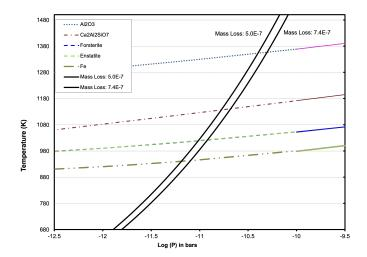


Figure 8. Pressure-temperature diagram for the space around RT Vir. The dark lines with labels show the PT-space occupied by RT Vir based on different calculations of the expansion velocity and dust mass-loss rate ($M_{\odot}yr^{-1}$ Olofsson et al. 2002; Loup et al. 1993). Dashed and dotted lines indicate the PT conditions required for certain minerals to condense out of the circumstellar material, extrapolated from data published in Lodders & Fegley (1999).

models for most AGB stars. However, our models suggest that dust around RT Vir is distant, and cool (\sim 330K at the innermost boundary). Since our models indicate the presence of cool, distant dust shells rather than compact, warm dust, this may suggest a slowdown in dust production at RT Vir.

Marengo et al. (2001) found that many AGB stars, particularly non-Mira variables, are best characterized by cooler inner dust temperatures. As an SRb variable, RT Vir may follow this trend.

If RT Vir was currently losing mass, one might expect to see hotter dust. Using the stellar luminosity and the theoretical condensation temperatures for common dust species (see Figure 8) we can calculate the distance at which dust should form as follows:

$$r = \sqrt{(1-A) * \frac{L_*}{16\pi\sigma T_{cond}^4}}$$
 (2)

Where A is the albedo of the dust, L_* is the stellar luminosity in Watts, and $T_{\rm cond}$ is the condensation temperature of the dust. If we take $L_* = 5000 L_{\odot}$ (Brand et al. 2020), $T_{\rm inner} = 1100\,K$, and A = 0.5 we can get a rough estimate of the dust formation distance: $r = 4.7 \times 10^7 {\rm km} = 3.14 {\rm AU}$. Evidently, this is far closer to the stellar surface than our modeled shells ($r \approx 2.23 \times 10^{10} {\rm km} = 149\,{\rm AU}$). The temperature $T_{\rm inner} = 1100\,K$ was selected based on Figure 8, which

indicates that ${\rm Al_2O_3}$ is expected to condense at $\sim 1350\,{\rm K}$ for RT Vir assuming thermodynamic equilibrium. However, as will be discussed in § 5.6, dust nucleation probably requires the outflowing gas to achieve supersaturation before dust can nucleate. To account for this effect, a slightly lower temperature — several hundred degrees cooler — was selected. The range of potential condensation temperatures T_{cond} depends on the composition of the gas, the mass-loss rate, the expansion velocity and the temperature of the star. For the common Mg-rich/iron-poor silicates (forsterite, enstatite), the thermodynamic equilibrium temperature does not drop much below 1000 K. Even when considering supersaturation requirements, T_{cond} or T_{inner} should be above 800 K. Our modeled T_{inner} is only 330 K

5.6. Dust Formation

There are multiple competing (or at least different) theoretical models of dust formation in the stellar outflows around AGB stars. One, and potentially the most intuitive is a model of thermodynamic equilibrium condensation. Lodders & Fegley (1999) have calculated the condensation temperatures and pressures of various silicates as well as Al-bearing minerals thought to be present in C & O-rich AGB outflows. Figure 8 uses these condensation properties for Al₂O₃, calcium aluminosilicate, enstatite, forsterite, and iron. It should follow then, that when the pressure-temperature space around an AGB star intersects the condensation pressure and temperature for a mineral, dust grains of that substance should start condensing so long as the elements that compose it are suitably abundant.

In contrast to forming at thermodynamic equilibrium dust grains may also form under conditions of super-saturation (e.g., Nuth & Hecht 1990; Gail & Sedlmayr 1999). In this case the outflowing gas cools, reaching a state of supersaturation before slow-forming mineral condensates can produce significant dust emission (Gail & Sedlmayr 1999). Al₂O₃, having the highest condensation temperature in O-rich AGB outflows, will have the longest time to form grains that can become the nuclei for silicate mantles to grow atop (Gail & Sedlmayr 1998).

Nuth & Hecht (1990) suggested that dust grains form around AGB stars by quickly condensing out of the supersaturated circumstellar vapor into 'chaotic silicates'. Within this chaotic grain, Si, Al, and other metals would not be fully oxidized, and since Al has the highest reduction potential, it would oxidize preferentially, even converting $Al + SiO \rightarrow AlO + Si$ (Stencel et al. 1990). It follows then, that in an O poor environment, Al will oxidize first, and may remove most of the free O in the

environment. In this case, there will be less SiO to form silicate grains or mantles atop Al_2O_3 , resulting in a lack of the associated emission at 10 and $20 \,\mu m$.

5.7. Epochs of Dust Formation

With these hypotheses of dust formation in mind, we can turn our attention back to our modeled dust shells around RT Vir. Our two modeled dust shells are likely indicative of two separate epochs of dust formation in the outflow of RT Vir. Since the outer shell is modeled using crystalline material, it likely formed closer to the star, and cooled slower, giving the Al₂O₃ time to anneal in the outflow. This could occur if the grains formed at thermodynamic equilibrium, or in a supersaturated gas, so long as the grains stayed at a high enough temperature (1100–1300 K, which include the temperatures at which Pecharromán et al. (1999) annealed their bayerite samples) for long enough to anneal (e. g. Gail & Sedlmayr 1999). The inner shell likely cooled faster, and could form amorphous grains, or amorphous mantles. In this case it is less likely that all grains formed at thermodynamic equilibrium, and more likely that grains condensed directly out of a supersaturated outflow at lower temperatures, or that amorphous mantles grew on top of crystalline or amorphous nuclei (Stencel et al. 1990; Gail & Sedlmayr 1999). In this case, the composition and crystallinity of the dust shells depend explicitly on the mass-loss rate of RT Vir, which governs the PT environment in the outflow (see Figure 8).

Alternatively, if the dust around RT Vir formed primarily as chaotic grains (e. g. Stencel et al. 1990), then the C/O ratio would drive the dust distribution and makeup over the stellar mass-loss rate. The enhanced abundance of Al₂O₃ compared to cosmic silicate (especially in the outer shell) is best explained as a function of high C/O ratio. If Al₂O₃ dust condenses before other dust species then the abundance of free oxygen to form silicates would be depleted. Additionally, in chaotic grains Al₂O₃ may form preferentially due to its high reduction potential compared to that of SiO₂ (e.g. Stencel et al. 1990). In either case, since C/O is high, Al₂O₃ may reduce the amount of free O atoms in the outflow, enough to prevent other O-bearing minerals (FeO, SiO₂, etc...) from condensing in great abundance. In the case of chaotic grain formation, a decrease in the C/O ratio could explain the shift in grain chemistry between the shells of our models.

One phenomenon that can decrease an AGB stars C/O is carbon burning in the star's envelope. In more massive AGB stars ($M > 4.0 \, M_{\odot}$), the bottom of the outer stellar envelope can begin the CNO cycle, consuming carbon during the third dredge up period in a

process called hot bottom burning (HBB; described in Boothroyd et al. 1993). As carbon is consumed in the stellar envelope, the C/O ratio may decrease over time, which is not what we expect for lower mass AGB stars. This decrease in C/O may account for the changes between dust shells in our models of RT Vir. If the outer shell formed when the circumstellar material had C/O greater than when the inner shell formed, it may suggest that the outer shell formed as chaotic silicates. Then, as C/O decreased as HBB occurred in the star, increased O abundance would encourage the formation of silicates and other oxides.

However, this can only be true if RT Vir is indeed greater than $\sim 4 \mathrm{M}_{\odot}$. We found one estimate of RT Vir's mass from Yates et al. (2002) at $1.5 M_{\odot}$ (too small to initiate HBB). However, no description of a method or citation for this number are given, and thus calls into question the reliability of this mass estimate. If RT Vir is less than $\sim 4 \rm{M}_{\odot}$, considering the C/O ratio as the determining factor in dust species formation would be difficult to justify. In this case the mass-loss rate would drive the change in composition between the outer and inner shells. In this case, Al₂O₃ in the outer shell may have formed during a period of low mass-loss rate, when the circumstellar envelope had enough pressure to form dust, but was too hot for anything other than Al₂O₃ to condense. After the circumstellar material cooled enough for other materials to condense, the pressure may have been too low to support significant formation of silicate mantles on Al_2O_3 grains or any other oxides. If the mass-loss rate increased between the formation of the outer and inner shells, the pressure could have stayed high enough to form silicate mantles and other oxides at temperatures below ~ 1100 K.

6. CONCLUSIONS

We have presented DUSTY modeling of the circumstellar dust of O-rich AGB star RT Vir. Our modeling was matched visually to IR SEDs for RT Vir. Our models suggest a pair of distant & cool shells of dust with low optical depths. The inner, younger shell in our best fit model has composition composed primarily of silicates and Al_2O_3 with additional components of FeO and metallic Fe. The outer, older shell is modeled entirely using a mixture of Al_2O_3 polymorphs, primarily θ -Al₂O₃. From this modeling we can assert the following:

- 1. RT Vir's circumstellar material is cold and distant compared to other O-rich AGB stars.
- 2. The distances from the star to our modeled dust shells are consistent with imaging at $70\,\mu\text{m}$ via Herschel.
- 3. There are two scenarios that could explain our results at RT Vir:
 - The differences in composition between the outer (older) and inner (younger) shells of dust suggest a change in the mass-loss rate. This would be consistent with theories of TE or supersaturation dust formation, which are driven by PT conditions over C/O ratio (e.g., Lodders & Fegley 1999; Gail & Sedlmayr 1999).
 - The compositional differences between the outer and inner shells of dust could be due to a decrease in C/O between the formation of the shells, which could be consistent with the formation of chaotic silicates which is driven by C/O more than PT conditions (e.g. Stencel et al. 1990). In this case RT Vir would have to have $M \ge 4M_{\odot}$.

6.1. Future Work

The interaction of the ISM with the astrosphere of RT Vir may act as a secondary source of energy contributing to FIR emission (see e.g. Young et al. 1993; Ueta et al. 2006). While outside the scope of this investigation, including an external factor like bow-shock interactions with dust and gas may enhance the accuracy of RT modeling.

Referring to Figure 3, the nominal gap between the inner and outer dust shells in our model is $\sim 1'$. Confirming this gap observationally would require interferometric measurements with an angular resolution of 0.2'' or better. Instruments like MIRC-X on the CHARA Interferometer (Mt Wilson) could observe the dust shell

in the near-infrared (NIR) with sufficient angular resolution to resolve such a dust gap. Similar observations at longer wavelengths (mid-IR) could be obtained with MATISSE on VLTI for southern hemisphere objects. Meanwhile, ALMA could trace the molecular gas emission.

We would like to acknowledge the support of the University of Texas at San Antonio. This research was funded by the National Science Foundation via NSF AST 2106926. B. A. Sargent would like to acknowledge funding via NASA APRA grant 80NSSC21K1468. We thank Dr. Kevin Volk for his M-star template used in our DUSTY models, and Dr. Joe Nuth for his wise counsel and expert advice as we revised the manuscript. We used the resources of Simbad: Strasbourg astronomical Data Center: https://simbad.u-strasbg.fr and NASA Infrared Science Archive (IRSA): https://irsa. ipac.caltech.edu/cgi-bin/Radar/nph-discovery in producing this research. Data used in this paper from IRSA can be accessed via https://doi.org/10.26131/IRSA1 (AllWISE) https://doi.org/10.26131/IRSA2 (2MASS);https://doi.org/10.26131/IRSA4 (IRAS) https://doi.org/10.26131/IRSA74 (HERSCHEL, MESS); https://doi.org/10.26131/IRSA181; (AKARI) https://doi.org/10.26131/IRSA524 (unWISE); https://doi.org/10.26131/IRSA544 (GAIA DR3). GALEX data used in this paper were obtained from the Mikulski Archive for Space Telescopes (MAST) at the Space Telescope Science Institute. The specific observations analyzed can be accessed via https://doi.org/10.17909/T9H59D. Finally, we would like to acknowledge that this investigation has been carried out on lands of the Jumanos, Coahuiltecan, Lipan Apache, and Tonkawa peoples.

Software: DUSTY (Nenkova et al. 1999), ProbabilityShapeDistributions (github.com/astroseandillon/AluminumOxide),

APPENDIX

A. PHOTOMETRY TABLE

Table 5. Photometry sources used in Figures 2 and 4

$\lambda(\mu m)$	Flux (Wm	⁻²) Catalog	Source	Observatory
0.1529	1.19E-16	J/ApJ/841/33/table1	Montez et al. (2017)	GALEX
0.1529	2.07E-16	J/ApJ/841/33/table1	Montez et al. (2017)	GALEX
0.2312	3.14E-16	I/353/gsc242	Lasker et al. (2008)	GALEX
0.2312	2.40E-16	J/ApJ/841/33/table1	Montez et al. (2017)	GALEX
0.2312	7.58E-16	J/ApJ/841/33/table1	Montez et al. (2017)	GALEX
0.3498	8.19E-13	II/379/smssdr4	Onken et al. (2024)	Sky Mapper
0.3498	8.77E-13	II/379/smssdr4	Onken et al. (2024)	Sky Mapper
0.3519	2.43E-12	I/353/gsc242	Lasker et al. (2008)	SDSS
0.3519	2.41E-12	V/154/sdss16	Ahumada et al. (2020)	SDSS
0.3519	4.01E-12	V/154/sdss16	Ahumada et al. (2020)	SDSS
0.3871	2.50E-12	II/379/smssdr4	Onken et al. (2024)	Sky Mapper
0.3871	2.54E-12	II/379/smssdr4	Onken et al. (2024)	Sky Mapper
0.4020	1.37E-09	I/358/varisum	Gaia Collaboration (2022)	Gaia DR3
0.4203	2.69E-12	$I/239/hip_main$	ESA (1997)	Hipparcos
0.4203	2.49E-12	I/275/ac2002	Urban et al. (1998)	Hipparcos
0.4442	2.54E-12	I/305/out	Lasker et al. (2008)	DSS
0.4442	4.00E-12	I/305/out	Lasker et al. (2008)	DSS
0.4442	3.92E-12	V/137D/XHIP	Anderson & Francis (2012)	Hipparcos
0.4442	2.79E-12	II/336/apass9	Henden et al. (2015)	APASS
0.4442	2.20E-12	I/342/f3	Andruk et al. (2016)	UCAC
0.4442	3.27E-12	J/MNRAS/463/4210 /ucac4rpm	Nascimbeni et al. (2016)	UCAC
0.4442	3.78E-12	IV/38/tic	Stassun et al. (2019)	TESS
0.4772	3.15E-12	II/349/ps1	Chambers et al. (2016)	Pan-STARRS
0.4772	8.76E-12	II/349/ps1	Chambers et al. (2016)	Pan-STARRS
0.4820	3.12E-12	I/353/gsc242	Lasker et al. (2008)	SDSS
0.4820	2.04E-12	II/336/apass9	Henden et al. (2015)	SDSS
0.4820	3.61E-12	V/154/sdss16	Ahumada et al. (2020)	SDSS
0.4820	3.62E-12	V/154/sdss16	Ahumada et al. (2020)	SDSS
0.4968	1.02E-11	II/379/smssdr4	Onken et al. (2024)	Sky Mapper
0.4968	1.13E-11	II/379/smssdr4	Onken et al. (2024)	Sky Mapper
0.5036	1.15E-11	I/350/gaiaedr3	Gaia Collaboration et al. (2021) Gaia
0.5319	8.72 E- 12	$I/239/hip_main$	ESA (1997)	Hipparcos
0.5470	1.01E-11	I/360/syntphot	Gaia Collaboration (2022)	Gaia
0.5537	2.71E-11	II/122B/merged	Mermilliod (1987)	Various
0.5537	9.33E-12	$I/239/hip_main$	ESA (1997)	Hipparcos
0.5537	1.48E-11	I/338/kmac3	Karbovsky et al. (2016)	AOTS
0.5537	9.20E-12	J/MNRAS/463/4210 /ucac4rpm	Nascimbeni et al. (2016)	UCAC
0.5537	7.41E-12	II/366/catalog	Jayasinghe et al. (2018)	ASAS-SN
0.5537	9.61E-12	IV/38/tic	Stassun et al. (2019)	TESS
0.5822	1.94E-10	I/350/gaiaedr3	Gaia Collaboration et al. (2021) Gaia

series Table 5 continued

$\lambda(\mu m)$	Flux (Wm	Table 5 continued Catalog	Source	Observatory
0.6041	2.79E-11	II/379/smssdr4	Onken et al. (2024)	Sky Mapper
0.6041	5.96E-11	II/379/smssdr4	Onken et al. (2024)	Sky Mapper
0.6126	2.58E-11	II/349/ps1	Chambers et al. (2016)	Pan-STARRS
0.6126	6.64E-11	II/349/ps1	Chambers et al. (2016)	Pan-STARRS
0.6226	1.72E-11	I/345/gaia2	Gaia Collaboration et al. (2018	
0.6247	2.54E-11	I/353/gsc242	Lasker et al. (2008)	SDSS
0.6247	1.90E-11	V/154/sdss16	Ahumada et al. (2020)	SDSS
0.6247	1.92E-11	V/154/sdss16	Ahumada et al. (2020)	SDSS
0.6247	2.80E-11	I/360/syntphot	Gaia Collaboration (2022)	SDSS
0.6469	7.11E-11	I/360/syntphot	Gaia Collaboration (2022)	Gaia
0.6730	1.46E-11	I/353/gsc242	Lasker et al. (2008)	Gaia
0.6730	1.46E-11	J/ApJ/867/105/refcat2	Tonry et al. (2018)	Gaia
0.6730	1.43E-11	J/A+A/623/A72/hipgpma	Kervella et al. (2019)	Gaia
0.7480	3.57E-10	II/349/ps1	Chambers et al. (2016)	Pan-STARRS
0.7621	4.97E-10	I/350/gaiaedr3	Gaia Collaboration et al. (2021	
0.7635	4.62E-19	I/353/gsc242	Lasker et al. (2008)	SDSS
0.7635	1.17E-12	I/353/gsc242	Lasker et al. (2008)	SDSS
0.7635	4.61E-19	V/154/sdss16	Ahumada et al. (2020)	SDSS
0.7635	1.92E-12	V/154/sdss16	Ahumada et al. (2020)	SDSS
0.7635	1.25E-09	I/360/syntphot	Gaia Collaboration (2022)	SDSS
0.7713	4.89E-11	II/379/smssdr4	Onken et al. (2024)	Sky Mapper
0.7713	8.62E-11	II/379/smssdr4	Onken et al. (2024)	Sky Mapper
0.7713	1.58E-10	II/379/smssdr4 II/379/smssdr4	Onken et al. (2024)	Sky Mapper
0.7713	1.87E-10	II/379/smssdr4	Onken et al. (2024)	Sky Mapper
0.8652	9.84E-10	II/349/ps1	Chambers et al. (2016)	Pan-STARRS
0.9018	1.16E-11	I/353/gsc242	Lasker et al. (2008)	SDSS
0.9018	1.65E-11	V/154/sdss16	Ahumada et al. (2020)	SDSS
0.9596	1.61E-09	II/349/ps1	Chambers et al. (2016)	Pan-STARRS
1.2390	3.47E-09	I/280B/ascc	Kharchenko (2001)	2MASS
1.2590 1.2500	3.47E-09 3.53E-09	II/246/out	Cutri et al. (2003)	2MASS
1.2632	3.64E-09	J/ApJS/190/203/var	Price et al. (2010)	COBE
1.6300	4.36E-09	II/246/out	Cutri et al. (2003)	2MASS
1.6495	4.35E-09	I/280B/ascc	Kharchenko (2001)	2MASS
2.1638	4.35E-09 3.14E-09	I/280B/ascc	Kharchenko (2001)	2MASS 2MASS
2.1030		II/246/out	Cutri et al. (2003)	
	3.00E-09	J/ApJS/190/203/var	Price et al. (2010)	2MASS
$2.2213 \\ 2.7001$	3.03E-09	II/161/catalog	Sweeney & Richardson (1995)	$\begin{array}{c} \text{COBE} \\ \text{TMSS} \end{array}$
3.3500	2.13E-09	, , =	Lasker et al. (2008)	
	1.44E-10	I/353/gsc242		WISE
3.3500	5.08E-11	II/311/wise	Cutri et al. (2012) Abrahamyan et al. (2015)	WISE
3.3500	5.06E-11	II/338/catalog		WISE
3.3500	1.10E-09	II/363/unwise	Schlafly et al. (2019)	WISE
3.5221	1.18E-09	J/ApJS/190/203/var	Price et al. (2010)	COBE
4.6000	5.68E-11	I/353/gsc242	Lasker et al. (2008)	WISE
4.6000	6.36E-11	II/311/wise	Cutri et al. (2012)	WISE
4.6000	6.40E-11	II/338/catalog	Abrahamyan et al. (2015)	WISE
4.6000	7.35E-10	II/363/unwise	Schlafly et al. (2019)	WISE
4.8896	4.73E-10	J/ApJS/190/203/var	Price et al. (2010)	COBE
8.6100	1.86E-10	II/297/irc	Ishihara et al. (2010)	AKARI

series Table 5 continued

$\lambda(\mu m)$	Flux (Wm	²) Catalog	Source	Observatory
11.559	5.95E-11	I/353/gsc242	Lasker et al. (2008)	WISE
11.559	8.88E-11	II/311/wise	Cutri et al. (2012)	WISE
11.590	1.43E-10	II/156A/main	Moshir & et al. (1990)	IRAS
11.590	1.51E-10	I/270/cpirss01	Hindsley & Harrington (1994)	IRAS
11.590	2.83E-13	V/98/msx	Egan & Price (1996)	IRAS
11.590	1.03E-10	$\rm J/MNRAS/471/770/table2$	McDonald et al. (2017)	IRAS
18.389	5.29E-11	II/297/irc	Ishihara et al. (2010)	AKARI
22.090	2.18E-11	I/353/gsc242	Lasker et al. (2008)	WISE
22.090	3.04E-11	II/311/wise	Cutri et al. (2012)	WISE
23.880	3.44E-11	II/156A/main	Moshir & et al. (1990)	IRAS
23.880	3.60E-11	I/270/cpirss01	Hindsley & Harrington (1994)	IRAS
23.880	2.56E-11	$\rm J/MNRAS/471/770/table2$	McDonald et al. (2017)	IRAS
61.849	2.19E-12	II/156A/main	Moshir & et al. (1990)	IRAS
61.849	2.40E-12	J/A+AS/93/121/table4	Nyman et al. (1992)	IRAS
61.849	2.41E-12	I/270/cpirss01	Hindsley & Harrington (1994)	IRAS
101.94	5.55E-13	II/125/main	Helou & Walker (1988)	IRAS
101.94	5.89E-13	II/156A/main	Moshir & et al. (1990)	IRAS
101.94	5.59E-13	J/A+A/629/A94/table1	Díaz-Luis et al. (2019)	IRAS

REFERENCES

- Abrahamyan, H. V., Mickaelian, A. M., & Knyazyan, A. V. 2015, Astronomy and Computing, 10, 99, doi: 10.1016/j.ascom.2014.12.002
- Ahumada, R., Allende Prieto, C., Almeida, A., et al. 2020, ApJS, 249, 3, doi: 10.3847/1538-4365/ab929e
- Anderson, E., & Francis, C. 2012, Astronomy Letters, 38, 331, doi: 10.1134/S1063773712050015
- Andriantsaralaza, M., Ramstedt, S., Vlemmings, W. H. T., & De Beck, E. 2022, A&A, 667, A74, doi: 10.1051/0004-6361/202243670
- Andruk, V. M., Pakuliak, L. K., Golovnia, V. V., et al. 2016, Kinematics and Physics of Celestial Bodies, 32, 260, doi: 10.3103/S0884591316050032
- Bains, I., Cohen, R. J., Louridas, A., et al. 2003, MNRAS, 342, 8, doi: 10.1046/j.1365-8711.2003.06245.x
- Begemann, B., Dorschner, J., Henning, T., et al. 1997, ApJ, 476, 199, doi: 10.1086/303597
- Berruyer, N., & Frisch, H. 1983, A&A, 126, 269 Bladh, S., & Höfner, S. 2012, A&A, 546, A76,
- doi: 10.1051/0004-6361/201219138
- Bohren, C. F., & Huffman, D. R. 1998, Absorption and Scattering of Light by Small Particles (John Wiley & Sons, Ltd),
- doi: https://doi.org/10.1002/9783527618156.fmatter
- Boothroyd, A. I., Sackmann, I. J., & Ahern, S. C. 1993, ApJ, 416, 762, doi: 10.1086/173275

- Brand, J., Engels, D., & Winnberg, A. 2020, /aap, 644, doi: https://doi.org/10.1051/0004-6361/202039157
- Chambers, K. C., Magnier, E. A., Metcalfe, N., et al. 2016, arXiv e-prints, arXiv:1612.05560, doi: 10.48550/arXiv.1612.05560
- Claussen, M. J., Sjouwerman, L. O., Rupen, M. P., et al. 2011, The Astrophysical Journal Letters, 739, L5, doi: 10.1088/2041-8205/739/1/L5
- Cox, N. L. J., Kerschbaum, F., van Marle, A. J., et al. 2012, A&A, 537, A35, doi: 10.1051/0004-6361/201117910
- Cutri, R. M., Skrutskie, M. F., van Dyk, S., et al. 2003,
 VizieR Online Data Catalog: 2MASS All-Sky Catalog of
 Point Sources (Cutri+ 2003), VizieR On-line Data
 Catalog: II/246. Originally published in: University of
 Massachusetts and Infrared Processing and Analysis
 Center, (IPAC/California Institute of Technology) (2003)
- Cutri, R. M., Wright, E. L., Conrow, T., et al. 2012, Explanatory Supplement to the WISE All-Sky Data Release Products, Explanatory Supplement to the WISE All-Sky Data Release Products
- de Graauw, T., Haser, L. N., Beintema, D. A., et al. 1996, A&A, 315, L49
- Díaz-Luis, J. J., Alcolea, J., Bujarrabal, V., et al. 2019,
 A&A, 629, A94, doi: 10.1051/0004-6361/201936087
 Dougados, C., Rouan, D., & Lena, P. 1992, A&A, 253, 464
 Draine, B. T. 1981, ApJ, 245, 880, doi: 10.1086/158864

- —. 2003, ApJ, 598, 1017, doi: 10.1086/379118
- Ducati, J. R. 2002, VizieR Online Data Catalog: Catalogue of Stellar Photometry in Johnson's 11-color system., CDS/ADC Collection of Electronic Catalogues, 2237, 0 (2002)
- Egan, M. P., & Price, S. D. 1996, AJ, 112, 2862, doi: 10.1086/118227
- ESA, ed. 1997, ESA Special Publication, Vol. 1200, The HIPPARCOS and TYCHO catalogues. Astrometric and photometric star catalogues derived from the ESA HIPPARCOS Space Astrometry Mission
- Fabian, D., Henning, T., Jäger, C., et al. 2001, A&A, 378, 228, doi: 10.1051/0004-6361:20011196
- Freytag, B., & Höfner, S. 2023, A&A, 669, A155, doi: 10.1051/0004-6361/202244992
- Gaia Collaboration. 2022, VizieR Online Data Catalog:
 Gaia DR3 Part 4. Variability (Gaia Collaboration, 2022),
 VizieR On-line Data Catalog: I/358. Originally published in: Astron. Astrophys., in prep. (2022)
- Gaia Collaboration, Brown, A. G. A., Vallenari, A., et al. 2018, A&A, 616, A1, doi: 10.1051/0004-6361/201833051
- Gaia Collaboration, Brown, A. G. A., Vallenari, A., et al. 2021, A&A, 649, A1, doi: 10.1051/0004-6361/202039657
- Gail, H. P., & Sedlmayr, E. 1985, A&A, 148, 183
- —. 1998, Faraday Discussions, 109, 303, doi: 10.1039/a709290c
- —. 1999, A&A, 347, 594
- Gilman, R. C. 1969, ApJL, 155, L185, doi: 10.1086/180332
 Goldreich, P., & Scoville, N. 1976, ApJ, 205, 144, doi: 10.1086/154257
- Groenewegen, M. A. T., Waelkens, C., Barlow, M. J., et al. 2011, A&A, 526, A162, doi: 10.1051/0004-6361/201015829
- Gustafsson, B. 1998, Ap&SS, 255, 241, doi: 10.1023/A:1001106917321
- Habing, H. J., Tignon, J., & Tielens, A. G. G. M. 1994, A&A, 286, 523
- Helou, G., & Walker, D. W., eds. 1988, InfraredAstronomical Satellite (IRAS) Catalogs andAtlases. Volume 7: The Small Scale Structure Catalog.,Vol. 7
- Henden, A. A., Levine, S., Terrell, D., & Welch, D. L. 2015,
 in American Astronomical Society Meeting Abstracts,
 Vol. 225, American Astronomical Society Meeting
 Abstracts #225, 336.16
- Henning, T., Begemann, B., Mutschke, H., & Dorschner, J. 1995, A&AS, 112, 143
- Hindsley, R. B., & Harrington, R. S. 1994, AJ, 107, 280, doi: 10.1086/116852

- Höfner, S. 2009, in Astronomical Society of the Pacific Conference Series, Vol. 414, Cosmic Dust - Near and Far, ed. T. Henning, E. Grün, & J. Steinacker, 3, doi: 10.48550/arXiv.0903.5280
- Höfner, S., Bladh, S., Aringer, B., & Ahuja, R. 2016, A&A, 594, A108, doi: 10.1051/0004-6361/201628424
- Höfner, S., & Olofsson, H. 2018, A&A Rv, 26, 1, doi: 10.1007/s00159-017-0106-5
- Imai, H., Shibata, K. M., Marvel, K. B., et al. 2003, The Astrophysical Journal, 590, 460, doi: 10.1086/374887
- Ishihara, D., Onaka, T., Kataza, H., et al. 2010, A&A, 514, A1, doi: 10.1051/0004-6361/200913811
- Ivezic, Z., & Elitzur, M. 1995, ApJ, 445, 415, doi: 10.1086/175707
- Jayasinghe, T., Kochanek, C. S., Stanek, K. Z., et al. 2018, MNRAS, 477, 3145, doi: 10.1093/mnras/sty838
- Joy, A. H. 1942, ApJ, 96, 344, doi: 10.1086/144469
- Karbovsky, V. L., Lazorenko, P. F., Buromsky, M. I., Kasjan, S. I., & Svachii, L. N. 2016, Kinematics and Physics of Celestial Bodies, 32, 207, doi: 10.3103/S0884591316040048
- Kawada, M., Baba, H., Barthel, P. D., et al. 2007, PASJ, 59, S389, doi: 10.1093/pasj/59.sp2.S389
- Kervella, P., Arenou, F., Mignard, F., & Thévenin, F. 2019, A&A, 623, A72, doi: 10.1051/0004-6361/201834371
- Kessler, M. F., Steinz, J. A., Anderegg, M. E., et al. 1996, A&A, 315, L27
- Kharchenko, N. V. 2001, Kinematika i Fizika Nebesnykh Tel, 17, 409
- Kim, J., Cho, S.-H., Oh, C. S., & Byun, D.-Y. 2010, ApJS, 188, 209, doi: 10.1088/0067-0049/188/1/209
- Krishna Swamy, K. S. 2005, Dust in the universe: similarities and differences, Vol. 7 (World Scientific Publishing Co. Pte. Ltd)
- Krügel, E. 2008, An Introduction to the Physics of Interstellar Dust (Taylor & Francis)
- Kudashkina, L. S., & Andronov, I. L. 2022, Odessa Astronomical Publications, 35, 41, doi: 10.18524/1810-4215.2022.35.268674
- Kwok, S. 1975, ApJ, 198, 583, doi: 10.1086/153637
- -.. 2004, Nature, 430, 985, doi: 10.1038/nature02862
- Lasker, B. M., Lattanzi, M. G., McLean, B. J., et al. 2008, AJ, 136, 735, doi: 10.1088/0004-6256/136/2/735
- Little-Marenin, I. R., & Little, S. J. 1988, ApJ, 333, 305, doi: 10.1086/166747
- —. 1990, AJ, 99, 1173, doi: 10.1086/115406
- Lodders, K., & Fegley, B., J. 1999, in Asymptotic Giant Branch Stars, ed. T. Le Bertre, A. Lebre, & C. Waelkens, Vol. 191, 279

- Loup, C., Forveille, T., Omont, A., & Paul, J. F. 1993, A&AS, 99, 291
- Marengo, M., Ivezić, Ž., & Knapp, G. R. 2001, MNRAS, 324, 1117, doi: 10.1046/j.1365-8711.2001.04399.x
- Martin, D. C., Fanson, J., Schiminovich, D., et al. 2005, ApJL, 619, L1, doi: 10.1086/426387
- Mathis, J. S., Rumpl, W., & Nordsieck, K. H. 1977, ApJ, 217, 425, doi: 10.1086/155591
- Matsuura, M., Yamamura, I., Murakami, H., Freund,
 M. M., & Tanaka, M. 1999, A&A, 348, 579,
 doi: 10.48550/arXiv.astro-ph/9906264
- Mauron, N., & Huggins, P. J. 2006, A&A, 452, 257, doi: 10.1051/0004-6361:20054739
- —. 2010, A&A, 513, A31,doi: 10.1051/0004-6361/200913970
- Mayer, A., Jorissen, A., Kerschbaum, F., et al. 2011, in
 Astronomical Society of the Pacific Conference Series,
 Vol. 445, Why Galaxies Care about AGB Stars II:
 Shining Examples and Common Inhabitants, ed.
 F. Kerschbaum, T. Lebzelter, & R. F. Wing, 351
- McDonald, I., Zijlstra, A. A., & Watson, R. A. 2017, MNRAS, 471, 770, doi: 10.1093/mnras/stx1433
- Mermilliod, J. C. 1987, A&AS, 71, 413
- Min, M., Hovenier, J. W., & de Koter, A. 2003, A&A, 404, 35, doi: 10.1051/0004-6361:20030456
- Molster, F. J., Waters, L. B. F. M., & Tielens, A. G. G. M. 2002a, A&A, 382, 222, doi: 10.1051/0004-6361:20011551
- Molster, F. J., Waters, L. B. F. M., Tielens, A. G. G. M., Koike, C., & Chihara, H. 2002b, A&A, 382, 241, doi: 10.1051/0004-6361:20011552
- Montez, Rodolfo, J., Ramstedt, S., Kastner, J. H., Vlemmings, W., & Sanchez, E. 2017, ApJ, 841, 33, doi: 10.3847/1538-4357/aa704d
- Morris, M., Sahai, R., Matthews, K., et al. 2006, in Planetary Nebulae in our Galaxy and Beyond, ed. M. J. Barlow & R. H. Méndez, Vol. 234, 469–470, doi: 10.1017/S1743921306003784
- Moshir, M., & et al. 1990, IRAS Faint Source Catalogue, 0 Nascimbeni, V., Piotto, G., Ortolani, S., et al. 2016, MNRAS, 463, 4210, doi: 10.1093/mnras/stw2313
- Nenkova, M., Ivezic, Z., & Elitzur, M. 1999, in LPI
 Contributions, Vol. 969, Thermal Emission Spectroscopy
 and Analysis of Dust, Disks, and Regoliths, ed.
 A. Sprague, D. K. Lynch, & M. Sitko, 20
- Nuth, Joseph A., I., & Hecht, J. H. 1990, Ap&SS, 163, 79, doi: 10.1007/BF00639979
- Nyman, L. A., Booth, R. S., Carlstrom, U., et al. 1992, A&AS, 93, 121

- Olofsson, H., González Delgado, D., Kerschbaum, F., & Schöier, F. L. 2002, A&A, 391, 1053, doi: 10.1051/0004-6361:20020841
- Onken, C. A., Wolf, C., Bessell, M. S., et al. 2024, PASA, 41, e061, doi: 10.1017/pasa.2024.53
- Paladini, C., Klotz, D., Sacuto, S., et al. 2017, A&A, 600, A136, doi: 10.1051/0004-6361/201527210
- Pecharromán, C., Sobrados, I., Iglesias, J. E., González-Carreño, T., & Sanz, J. 1999, The Journal of Physical Chemistry B, 103, 6160, doi: 10.1021/jp983316q
- Perrin, G., Coudé du Foresto, V., Ridgway, S. T., et al. 1998, A&A, 331, 619
- Pickering, E. C., & Fleming, W. P. 1896, ApJ, 3, 296, doi: 10.1086/140219
- Pickles, A. J. 1985, ApJS, 59, 33, doi: 10.1086/191061
- Pilbratt, G. L., Riedinger, J. R., Passvogel, T., et al. 2010, A&A, 518, L1, doi: 10.1051/0004-6361/201014759
- Price, S. D., Smith, B. J., Kuchar, T. A., Mizuno, D. R., & Kraemer, K. E. 2010, ApJS, 190, 203, doi: 10.1088/0067-0049/190/2/203
- Randall, S. K., Trejo, A., Humphreys, E. M. L., et al. 2020, A&A, 636, A123, doi: 10.1051/0004-6361/201935787
- Sacuto, S., Ramstedt, S., Höfner, S., et al. 2013, A&A, 551, A72, doi: 10.1051/0004-6361/201220524
- Sahai, R., Huang, P. S., Scibelli, S., et al. 2022, ApJ, 929, 59, doi: 10.3847/1538-4357/ac568a
- Sahai, R., & Stenger, B. 2023, AJ, 165, 229, doi: 10.3847/1538-3881/acccf2
- Sahai, R., Trauger, J. T., Watson, A. M., et al. 1998, ApJ, 493, 301, doi: 10.1086/305121
- Sandin, C., Mattsson, L., Chubb, K. L., Ergon, M., & Weilbacher, P. M. 2023, A&A, 677, A27, doi: 10.1051/0004-6361/202345841
- Sargent, B. A. 2018, ApJL, 866, L1, doi: 10.3847/2041-8213/aae085
- Schlafly, E. F., Meisner, A. M., & Green, G. M. 2019, ApJS, 240, 30, doi: 10.3847/1538-4365/aafbea
- Sharma, K., Prugniel, P., & Singh, H. P. 2016, A&A, 585, A64, doi: 10.1051/0004-6361/201526111
- Skrutskie, M. F., Cutri, R. M., Stiening, R., et al. 2006, AJ, 131, 1163, doi: 10.1086/498708
- Sloan, G. C., Goes, C., Ramirez, R. M., Kraemer, K. E., & Engelke, C. W. 2015, ApJ, 811, 45, doi: 10.1088/0004-637X/811/1/45
- Sloan, G. C., Kraemer, K. E., Goebel, J. H., & Price, S. D. 2003, ApJ, 594, 483, doi: 10.1086/376857
- Sloan, G. C., & Price, S. D. 1998, ApJS, 119, 141, doi: 10.1086/313156
- Speck, A. K., Barlow, M. J., Sylvester, R. J., & Hofmeister, A. M. 2000, A&AS, 146, 437, doi: 10.1051/aas:2000274

- Speck, A. K., Corman, A. B., Wakeman, K., Wheeler, C. H., & Thompson, G. 2009, ApJ, 691, 1202, doi: 10.1088/0004-637X/691/2/1202
- Speck, A. K., Pitman, K. M., & Hofmeister, A. M. 2015, ApJ, 809, 65, doi: 10.1088/0004-637X/809/1/65
- Stassun, K. G., Oelkers, R. J., Paegert, M., et al. 2019, AJ, 158, 138, doi: 10.3847/1538-3881/ab3467
- Stencel, R. E., Nuth, Joseph A., I., Little-Marenin, I. R., & Little, S. J. 1990, ApJL, 350, L45, doi: 10.1086/185664
- Sweeney, L. H., & Richardson, T. 1995, VizieR Online Data
 Catalog: Equatorial Infrared Catalog (Sweeney+ 1990),
 VizieR On-line Data Catalog: II/161. Originally
 published in: Space Applications Corporation 1990
- Tonry, J. L., Denneau, L., Flewelling, H., et al. 2018, ApJ, 867, 105, doi: 10.3847/1538-4357/aae386
- Ueta, T., Torres, A. J., Izumiura, H., et al. 2018, Publications of the Astronomical Society of Japan, 71, 4, doi: 10.1093/pasj/psy130
- Ueta, T., Speck, A. K., Stencel, R. E., et al. 2006, ApJL, 648, L39, doi: 10.1086/507627
- Urban, S. E., Corbin, T. E., Wycoff, G. L., et al. 1998, AJ, 115, 1212, doi: 10.1086/300264
- van der Veen, W. E. C. J., Omont, A., Habing, H. J., & Matthews, H. E. 1995, A&A, 295, 445

- van Leeuwen, F. 2007, A&A, 474, 653, doi: 10.1051/0004-6361:20078357
- van Loon, J. T., Cioni, M. R. L., Zijlstra, A. A., & Loup, C. 2005, A&A, 438, 273, doi: 10.1051/0004-6361:20042555
- Vassiliadis, E., & Wood, P. R. 1993, ApJ, 413, 641, doi: 10.1086/173033
- Villaver, E., García-Segura, G., & Manchado, A. 2002a, ApJ, 571, 880, doi: 10.1086/340022
- Villaver, E., Manchado, A., & García-Segura, G. 2002b, ApJ, 581, 1204, doi: 10.1086/344250
- Wareing, C. J., Zijlstra, A. A., Speck, A. K., et al. 2006,
 MNRAS, 372, L63, doi: 10.1111/j.1745-3933.2006.00227.x
 Woitke, P. 2006, A&A, 460, L9,
 - doi: 10.1051/0004-6361:20066322
- Yamamura, I., Dominik, C., de Jong, T., Waters,L. B. F. M., & Molster, F. J. 2000, A&A, 363, 629
- Yates, J. A., Richards, A. M. S., & Gray, M. D. 2002, in Cosmic Masers: From Proto-Stars to Black Holes, ed. V. Migenes & M. J. Reid, Vol. 206, 298
- Young, K., Phillips, T. G., & Knapp, G. R. 1993, ApJ, 409, 725, doi: 10.1086/172702
- Zargarnezhad, H., Myers, R. J., Speck, A. K., & McFarland, J. A. 2023, Astronomy and Computing, 45, 100766, doi: 10.1016/j.ascom.2023.100766
- Zhang, B., Zheng, X., Reid, M. J., et al. 2017, The Astrophysical Journal, 849, 99, doi: 10.3847/1538-4357/aa8ee9